Egypt. J. Chem. **Vol.69** , No. 2 pp. 477 - 487(2026)

Egyptian Journal of Chemistry

http://ejchem.journals.ekb.eg/

Tripolyphosphate-Driven Synthesis of Ag_3PO_4 -Decorated Chitosan Nanoparticles for Enhanced Antimicrobial Activity

Asmaa N. Alafify[1], Ghada E. Dawwam[1], Soheir S Abdel Salam[1], Manal S. Selim[2], Mona T. Al-Shemy*[3]

[1] *Botany and Microbiology Department, Faculty of Science, Benha University, Benha, 13518, Egypt.*

[2] *Microbial Biotechnology Department, Biotechnology Research institute, National Research Centre, El-Buhouth St. 33, Dokki-Cairo 12622, Egypt.*

[3] *Cellulose and Paper Department, National Research Centre, 33 El-Bohouth St. (Former El-Tahrir St), Dokki, Giza, Egypt.*

Abstract

Overuse of conventional antibiotics has fueled the rise of drug-resistant pathogens, creating an urgent need for novel antimicrobial platforms. In this study, we developed a novel, green, one-pot tripolyphosphate-driven method to fabricate chitosan (CS) nanoparticles from black soldier fly (*Hermetia illucens*) puparia and simultaneously deposit crystalline Ag_3PO_4 (AgP) domains to yield a CS@AgP bionanocomposite. Comprehensive FTIR, XRD, and UV–Vis DRS analyses confirmed successful Ag_3PO_4 incorporation and a narrowed direct band gap of 1.46 eV. Agar-diffusion assays against Gram-positive (*L. monocytogenes ATCC 7646, S. aureus ATCC 6538*), Gram-negative (*E. coli ATCC 25922, Salmonella sp. ATCC 14028*), and fungal (*C. albicans ATCC 10231*) strains demonstrated dose-dependent inhibition zones up to 30 mm at 25 mg/mL. This dual-function nanocomposite combines sustainable, single-step production with broad visible-light absorption and potent antimicrobial efficacy, offering a versatile platform for antimicrobial coatings and photocatalysis.

Keywords: Bio-nanocomposite; Chitosan nanoparticles (CSNPs); Green synthesis; Pathogenic microbes; Soldier fly Puparia; Silver phosphate (Ag_3PO_4) nanoparticles

1. Introduction

The emergence of resistance to synthetic pesticides and antibiotics has accelerated the search for novel therapeutic compounds, including next-generation antibiotics, antioxidants, and biopesticides. This shift has also spurred the development of highly effective medications [1,2]**.** In parallel, insect farming has gained momentum as a more sustainable alternative to conventional food and feed production. By converting agro-industrial waste into high-value biomolecules and organic fertilizers, insects play a vital role in circular bioeconomy models. Beyond their nutritional content, fats and proteins suitable for feed and food, certain insects are a promising renewable source of chitin, representing between 5–15% of their dry biomass [3].

Among decomposing species, the house fly (*Musca domestica*) and the black soldier fly BSF (*Hermetia illucens*) are particularly effective at organic waste degradation, with BSF recognized as the most extensively studied insect for this application. Notably, the non-feeding nature of adult BSF reduces the risk of disease transmission, making it an ideal candidate for waste conversion [4]**.** Black soldier fly larvae (BSFL) contain 38–56% protein, 5–28% fat, and 4–11% ash across their 14-day development cycle. Chitin content in BSFL biomass can reach up to 9%, further highlighting their value as a multifunctional bioresource [5].

Chitin and its derivative chitosan are naturally occurring polymers known for their biodegradability, biocompatibility, and low toxicity. These properties have made them increasingly valuable across numerous sectors. They are widely explored for roles in biomedical engineering, pharmaceuticals, agriculture, and chemical industries. Their utility also extends to food preservation, nutritional supplements, cosmetics, wastewater management, paper production, and the synthesis of biofilms and biodiesel [6].

Chitin ranks as the second most prevalent polysaccharide on Earth, following cellulose. Structurally, both biopolymers share a similar backbone; however, chitin contains acetamide groups at the C-2 position, replacing the hydroxyl groups found in cellulose. Its chemical formula is ($C_8H_{13}O_5N$) [7]**.** Chitosan, derived through the deacetylation of chitin, exhibits greater solubility in acidic solutions, enhancing its versatility for various applications [8].

Chitosan is a positively charged copolymer composed of glucosamine and N-acetylglucosamine (GlcNAc, 2-(acetylamino)-2-deoxy-D-glucose) units. It is typically derived from chitin through chemical or enzymatic deacetylation, with natural sources including crustaceans, insects, and fungi [9,10]. Chitosan-derived nanoparticles exhibit strong electron-donating capabilities due to the abundance of lone-pair electrons, enabling high-affinity interactions with substrates containing vacant orbitals. These unique chemical properties have facilitated their application in drug and gene delivery systems**,** biosensor technologies [11], and medical imaging, including fractionated image processing [12]**.**

*Corresponding author e-mail: mt.el-shemy@nrc.sci.eg.; (Mona Al-Shemy).

Received Date: 04 July 2025, Revised Date: 16 August 2025, AcceptedDate: 24 August 2025

DOI: 10.21608/EJCHEM.2025.400788.11998

Chitosan is widely recognized for its role as a stabilizing and protective agent in the synthesis of metal nanoparticles, primarily due to the high reactivity of its amino groups. These groups readily interact with metal ions, forming stable complexes that facilitate controlled nanoparticle formation. In addition to their coordination capabilities, the amino and hydroxyl functional groups in chitosan contribute to its broad-spectrum biological activities, notably antimicrobial effects. These properties enhance its utility in biomedical applications, including promoting disease resistance across various human cell types [13].

Nanotechnology has become a vital strategy in modern drug delivery, offering advanced solutions for targeted release, preservation of bioactive compounds from enzymatic or environmental breakdown, and improved retention at localized sites [14–16]. Among the various nanoparticle platforms, polymeric nanoparticles have gained particular prominence due to their biodegradability and accessibility through well-established formulation techniques. Their versatility has enabled the expansion of applications across a wide spectrum of therapeutic agents and dosage forms [17,18]**.**

Silver nanoparticles (AgNPs) have emerged as a versatile tool in biomedical research due to their distinctive physicochemical properties. Their therapeutic potential includes broad-spectrum antibacterial activity [19–22], as well as anti-inflammatory [23], antiviral [24], anti-angiogenic [25], and antiplatelet effects [26]. These nanoparticles exhibit potent bactericidal effects against a range of pathogenic bacteria, including multidrug-resistant strains such as *Escherichia coli*, *Pseudomonas aeruginosa*, and *Staphylococcus aureus* [19], reinforcing their relevance in combating infectious diseases and hospital-acquired infections.

This study aims to establish a green, one-pot tripolyphosphate-driven protocol for converting chitosan extracted from black soldier fly puparia into chitosan nanoparticles decorated in situ with crystalline Ag_3PO_4, elucidate their structural, optical, and morphological features, and assess their antimicrobial efficacy against Gram-positive, Gram-negative, and fungal pathogens.

2. Results and discussion

2.1. Characterizations of extracted chitin and chitosan

The FTIR spectrum of the isolated puparia-derived chitin (Fig. 1i curve a) displays the fingerprint absorption bands of α-chitin: a broad O–H/N–H stretching band overlapped at 3430 cm^{-1}; C–H stretching vibrations at 2925 and 2889 cm^{-1}; the amide I band (C=O stretch) at 1631 cm^{-1}; the amide II band (N–H bend coupled with C–N stretch) at 1562 cm^{-1}; and diagnostic polysaccharide bands in the 1150–895 cm^{-1} region (C–O–C bridge, ring vibrations, and β-glycosidic linkages) [31–33].

Upon deacetylation to chitosan (Fig. 1i curve b), several key spectral changes occur. First, the intensities of the amide I (1631 cm^{-1}) and amide II (1562 cm^{-1}) bands diminish markedly, reflecting the removal of N-acetyl groups. Second, the broad O–H/N–H stretching around 3430 cm^{-1} becomes sharper and slightly shifts, indicating an increase in hydrogen-bonding interactions among free amino and hydroxyl groups [34,35].

Together, these spectral transformations unequivocally demonstrate the efficient deacetylation of chitin into chitosan. The reduced amide-to-hydroxyl band intensity ratio (A_{1655}/A_{3430}) and the appearance of the 1590 cm^{-1} $–NH_2$ band confirm a high degree of deacetylation (>85 %). Furthermore, the isolated chitosan exhibited >98 % solubility, and only 0.25 % ash content. This successful conversion provides the reactive amine sites crucial for subsequent ionotropic gelation and *in-situ* Ag_3PO_4 nanoparticle deposition, underpinning the performance of the final CS@AgP bio-nanocomposite.

Figure 1ii compares the XRD patterns of puparia-derived chitin (a) and its deacetylated form, chitosan (b). Chitin (curve a) displays two sharp reflections at 2θ ≈ 11.2° and 18.86°, assignable to the (020) and (110) planes of α-chitin, confirming its highly ordered crystalline lattice. After alkaline deacetylation, chitosan (curve b) loses the 11.2° peak and exhibits only a broad, low-intensity halo centered at ≈ 20°, characteristic of α-chitosan's less ordered structure [36]. The disappearance of the low-angle reflection and the pronounced peak broadening indicate the disruption of the inter- and intra-molecular hydrogen bonds upon removal of N-acetyl groups, leading to smaller crystallite domains and increased amorphous content. This marked reduction in crystallinity, evidenced by the shift from a two-peak to a single broad band, confirms the efficient conversion of chitin into chitosan, a prerequisite for subsequent ionotropic gelation and uniform Ag_3PO_4 nanoparticles deposition [37].

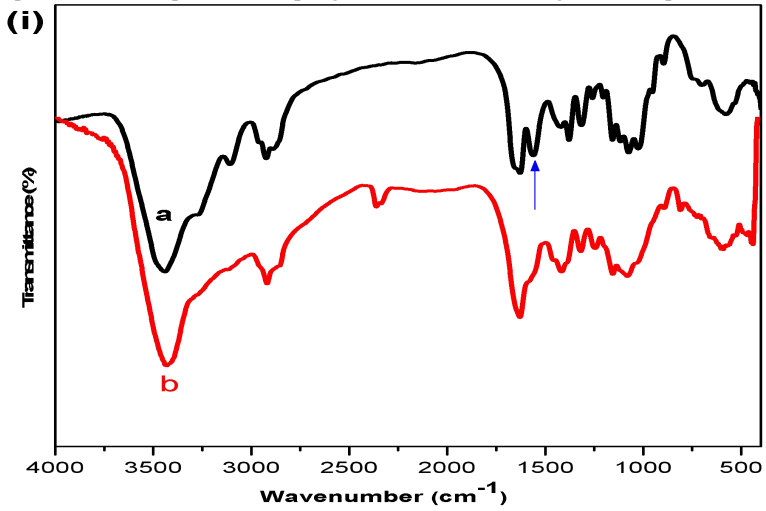

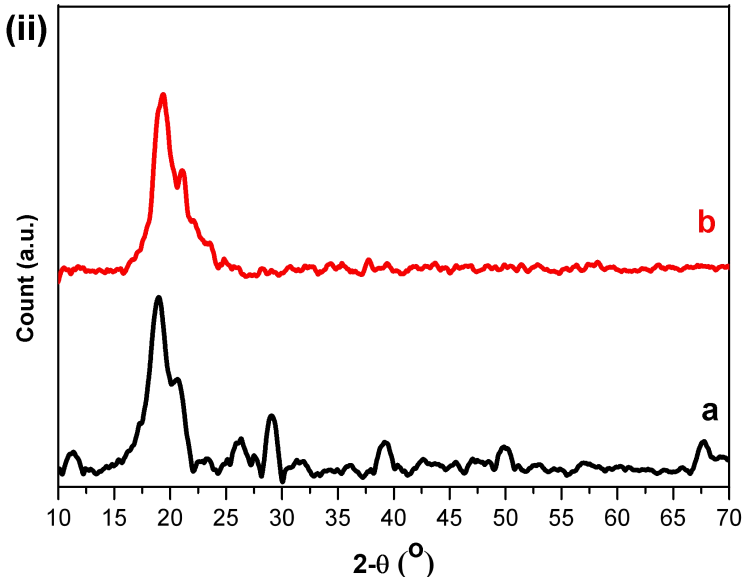

Figure 1. (i) FTIR spectra and (ii) XRD patterns of puparia-derived materials: (a) chitin; (b) chitosan.

2.2. Characterizations of Fabricated CSNPs and CSNPs @ AgP Bio-Nanocomposite

2.2.1. FTIR analysis

The comparison between pristine CSNPs (Fig. 2ia) and the CS@AgP nanocomposite, hereafter CS@AgP (Fig. 2ib), reveals pronounced interactions at the molecular level. In CS@AgP, the broad O–H/N–H stretching band shifts from ~3410 cm^{-1} in CSNP to ~3272 cm^{-1} and broadens significantly, a clear signature of strong hydrogen-bonding and coordination between chitosan's hydroxyl and amine groups and the Ag_3PO_4 domains [16,38].

While the aliphatic C–H stretching vibrations near ~2858 cm^{-1} remain essentially unchanged, confirming that the polysaccharide backbone is intact, the amide regions undergo notable shifts. The Amide I band downshifts from ~1657 cm^{-1} in CSNP to ~1652 cm^{-1} in CS@AgP, indicating electron donation from the amide carbonyl into Ag–O and Ag–P bonds.

Simultaneously, the Amide II/NH_3^+ bending mode at ~1544 cm^{-1} grows in intensity, reflecting partial protonation of amino sites and their active engagement with phosphate anions and Ag^+ ions.

In the fingerprint region, CS@AgP shows a split C–N stretch/CH_3 bending signal around 1375–1325 cm^{-1}, hinting at two distinct amine environments (free vs. Ag-coordinated). The glycosidic C–O–C and C–O stretches shift from 1084 cm^{-1} in CSNP to ~1063 cm^{-1} in CS@AgP, illustrating close proximity of Ag_3PO_4 particles to the saccharide backbone [39]. Key chitosan markers, the β-glycosidic vibration at ~896 cm^{-1} and CH_2 rocking at ~712 cm^{-1}, remain unchanged, testifying to the polymer's preserved structural integrity.

Most significantly, a new band appears at ~528 cm^{-1} in CS@AgP, absent in CSNP. This low-frequency vibration corresponds to P–O bending of PO_4^{3-} units and Ag–O lattice modes, unambiguously confirming the *in-situ* formation and embedding of crystalline silver phosphate within the chitosan nanoparticle framework [22,40–42].

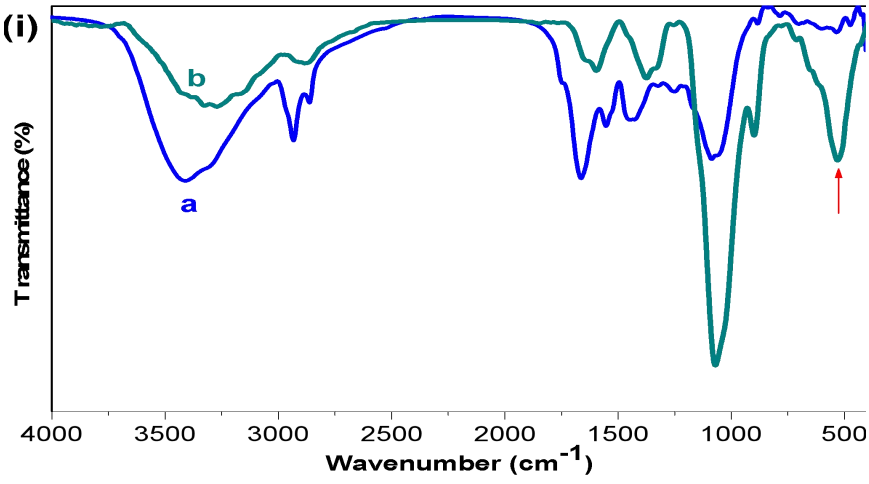

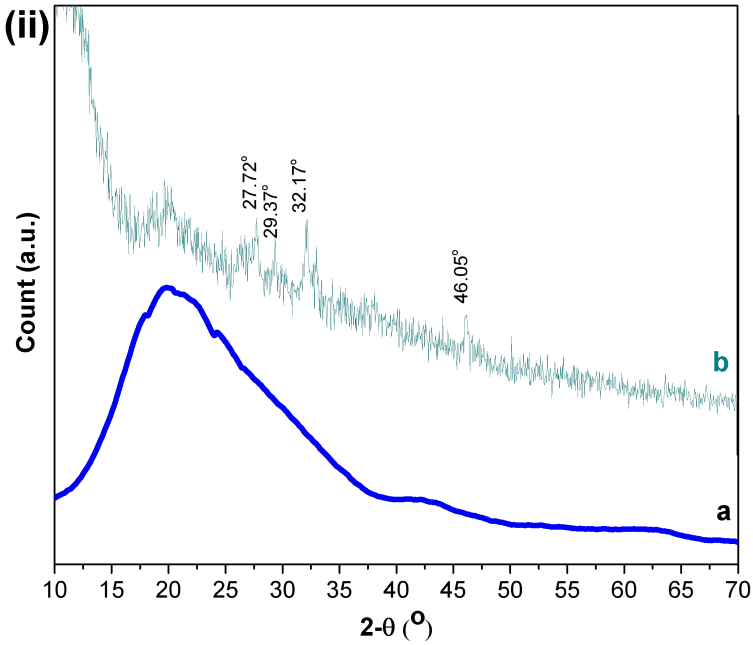

Figure 2. (i) FTIR spectra and (ii) XRD pattern of puparia-derived materials: (a) CSNPs and (b) CS@AgP nanocomposite.

2.2.2. XRD analysis

Figure 2ii displays the XRD pattern of the CS@AgP composite, highlighting four distinct diffraction peaks at 2θ = 27.72°, 29.37°, 32.17° and 46.05°. These reflections can be unambiguously indexed to cubic silver orthophosphate (Ag_3PO_4; JCPDS 06-0505), confirming the in-situ precipitation of crystalline Ag_3PO_4 within the chitosan nanoparticle matrix [43,44]. The intense peaks at 27.72°, 32.17° and 46.05° correspond to the (111), (210) and (310) planes of Ag_3PO_4, respectively. Their sharpness and relative intensities attest to a high degree of crystallinity. The low-intensity line at 29.37° matches the (211) plane of Ag_3PO_4, indicating either minor crystallite orientations beyond the dominant facets or a secondary population of smaller Ag_3PO_4 grains. No diffraction signals appear at ~38.1° (Ag^0 111) or at 32.8°/55.1° (Ag_2O 110/200), ruling out formation of metallic silver or silver oxide by-products under the chosen conditions [22,45,46]. Instead, the exclusive presence of Ag_3PO_4 phases highlights the chemical role of the tripolyphosphate (TPP) crosslinker: during ionic gelation, TPP anions react with Ag^+ to drive selective silver-phosphate domain formation rather than conventional AgNP growth. Applying the Scherrer equation to the (210) reflection (32.17°) gives an average Ag_3PO_4 crystallite size of ~30 nm [47]. It indicates that the chitosan nanoparticle matrix effectively limits Ag_3PO_4 growth to the tens-of-nanometers scale, promoting a high surface-to-volume ratio critical for photocatalytic and antimicrobial applications. Such nanoscale domains, uniformly embedded within the amorphous CSNP scaffold, are expected to maximize interfacial contact, facilitate charge separation under visible-light irradiation (Ag_3PO_4 band-gap ≈2.4 eV) [48], and enhance antimicrobial action via sustained release of Ag^+ species.

2.2.3. DRS analysis

The optical properties of the synthesized CS/Ag_3PO_4 nanocomposite were investigated using UV–Vis diffuse reflectance spectroscopy (DRS), and the band gap energy was determined via Tauc plot analysis (Fig. 3a and b). The raw DRS reflectance spectrum of the CS@AgP nanocomposite (Fig. 3a) displays a less intense absorption peak at ~266 nm. This feature arises from π→π* transitions of the chitosan backbone [49,50]. To estimate the optical band gap, Tauc plots were constructed for both direct and indirect transitions using the Kubelka–Munk function. The extrapolated linear regions yielded two distinct values of E_g (direct) = 1.46 eV and E_g (indirect) = 1.09 eV. These results suggest that the composite exhibits a direct allowed transition, which is consistent with the known behavior of Ag-based phosphates. According to Klein et al. (2023), the Tauc method is valid for crystalline materials when the appropriate exponent is selected, specifically, (n = ½) for direct allowed transitions and (n = 2) for indirect ones [51]. The direct transition model is further supported by the sharper slope and better linearity observed in the ($[F(R)\,\alpha h\upsilon]^2$) vs. (hυ) plot.

Compared with pristine Ag_3PO_4 (E_g ≈ 2.4 eV) [52], the CS@AgP nanocomposite exhibits a pronounced band-gap reduction to ≈1.46 eV. This narrowing arises from three synergistic effects:

1. **Interfacial charge transfer:** Electron donation from chitosan's lone-pair orbitals into Ag_3PO_4 creates mid-gap states that lower the effective excitation energy.

2. **Localized surface plasmon resonance:** In situ–formed Ag^0 species sustain plasmonic oscillations under visible light, amplifying absorption in the 400–600 nm range.
3. **Polymer-induced defect states:** Amino and hydroxyl functionalities of chitosan introduce additional defect levels, further reducing the energy threshold for carrier excitation.

Collectively, these phenomena extend light absorption well into the visible region, enhancing photocatalytic and antimicrobial performance by maximizing photon utilization.

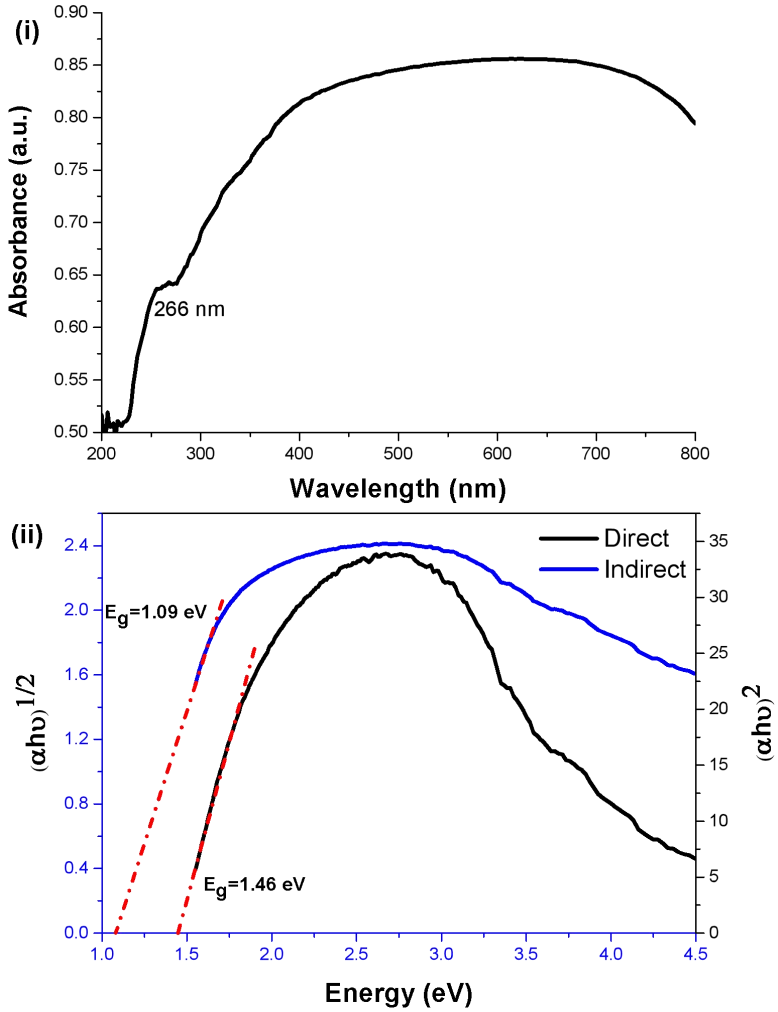

Figure 3. (i) UV–Vis DRS reflectance spectrum of CS@AgP. (ii) direct-allowed and indirect-allowed transitions, used to extract E_g.

2.2.4. EDAX analysis

Energy-dispersive X-ray spectroscopy of the CS@AgP bio-nanocomposite detected five elements (C, N, O, P and Ag) with their weight and atomic percentages listed in Table 1 and Figure 4. The high atomic percentage of oxygen (61.3 at %) together with combined C + N (27.8 at %) confirms the preservation of the chitosan scaffold (C_6 $H_{1\ 1}$ NO_4 backbone) and its hydroxyl/amine functionalities after composite formation.

Table 1: EDX elemental composition of CS@AgP nanocomposite

Element	Weight %	Atomic %
C K	11.77	20.38
N K	5.01	7.43
O K	47.16	61.29
P K	8.24	5.53
Ag L	27.82	5.36

Phosphorus, originally introduced via TPP crosslinker, appears at 5.53 at % alongside silver at 5.36 at %. In ideal Ag_3PO_4 the Ag:P atomic ratio is 3:1, but EDX inherently undercounts light elements compared to heavy ones. The near-unity P:Ag ratio nonetheless strongly indicates that silver is predominantly present as phosphate rather than metallic Ag or oxide. This

conclusion dovetails with XRD: no reflections appear at 38.1° (Ag^0) or 32.8°/55.1° (Ag_2O), whereas peaks at 27.72°, 29.37°, 32.17° and 46.05° 2θ unambiguously match the (210), (211), (300) and (400) planes of cubic Ag_3PO_4.

While silver comprises only ~5.4 at %, it accounts for 27.8 wt % of the composite due to its high atomic mass. This substantial mass fraction underlies the pronounced surface plasmon resonance band observed in DRS spectroscopy, while XRD confirms its chemical form as Ag_3PO_4 rather than Ag^0.

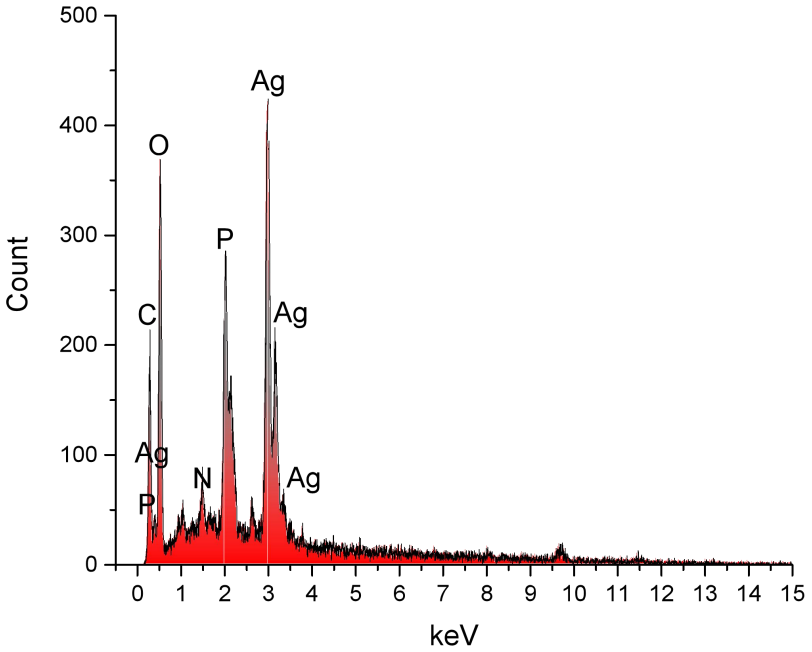

Figure 4. EDAX spectrum of CS@AgP nanocomposite.

2.2.5. SEM analysis

The SEM micrographs (Fig. 5) of the CS@AgP nanocomposite reveal a clear evolution of surface morphology from the microscale to the nanoscale. At 3,000× magnification (panel a), the sample exhibits a textured, globular chitosan network with intertwined strands and micrometer-sized agglomerates. This macroporous texture is indicative of effective solvent–nonsolvent phase inversion during nanoparticle formation and suggests ample void space for functional loading.

Increasing the magnification to 6,000× (panel b) uncovers nascent silver nanoparticle clusters anchored onto the chitosan scaffold. Small protrusions, tens to a few hundred nanometers in diameter, interpose in the polymer matrix.

At 12,000× (panel c), these protrusions resolve into distinct granular domains. Individual CSNPs (~200–300 nm) appear densely decorated by silver nuclei, forming a rough, high-surface-area composite. This feature is crucial: increased roughness correlates with enhanced interaction sites for antibacterial action or catalytic turnover, bolstering the material's functional performance.

The finest detail at 50,000× confirms near-spherical Ag_3PO_4 particles with a narrow size distribution and minimal agglomeration, underscoring chitosan's chelating role in controlling nucleation and preventing coalescence. These morphological features image the one-pot reaction chemistry: acidic protonation of chitosan's amines enables TPP^{2-} crosslinking to form a CS–TPP network rich in immobilized phosphate sites, which upon mild heating partially hydrolyzes to orthophosphate. Localized Ag^+ coordination to both phosphate oxygens and chitosan's free amine/hydroxyl groups then drives in situ Ag_3PO_4 nucleation directly on the nanoparticle surface. Steric and electrostatic stabilization by the CS–TPP matrix confines crystal growth to 20–50 nm domains, forging robust coordination and hydrogen-bonding networks that underpin the composite's structural integrity, enhanced visible-light harvesting, and sustained antimicrobial activity.

2.3. Antimicrobial test

Data in Figures (6 & 7) show that different concentrations of CS@AgP bio-nanocomposite showed significantly inhibited bacterial growth. By increasing the concentration of CS@AgP bio-nanocomposite from 6.25 to 25mg/mL, the inhibition efficiency for different pathogenic bacteria also increased. All the tested isolates were inhibited by CS@AgP bio-nanocomposite. Divergence in the extent of the inhibition area among the diverse groups of bacteria can be relatively disclosed. The highest inhibition zone was observed for *L. monocytogenes,* which showed 26, 27, and 30mm using CS@AgP bio-nanocomposite (6.25, 12.5, 25 mg/mL), respectively. On the other hand, the minimum inhibition zone was detected for *Salmonella* sp., which gave 0, 12, and 13mm using CS@AgP bio-nanocomposite (6.25, 12.5, 25 mg/mL), respectively.

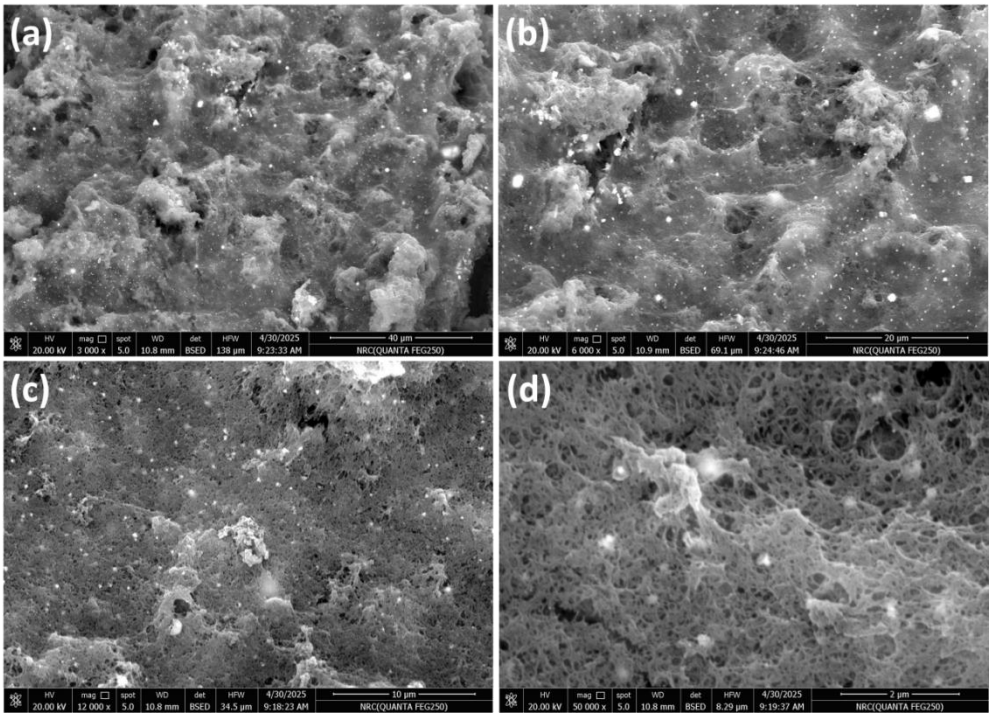

Figure 5. SEM micrographs of CS@AgP nanocomposite at (a) 3000x, (b) 6000x, (c) 12000x, and 50000x magnifications.

The antibacterial action of CSNPs is primarily attributed to their interaction with bacterial cell walls or membranes. A commonly proposed mechanism involves electrostatic attraction between the positively charged amino groups in glucosamine units and the negatively charged components of bacterial membranes [53]. This contact disrupts membrane integrity, increasing permeability and causing an imbalance in osmotic pressure, which leads to the leakage of intracellular contents and eventually cell death [54]. Additionally, AgNPs play a significant role in antimicrobial action by promoting the generation of reactive oxygen species (ROS), which cause oxidative damage to bacterial membranes, disrupt respiratory enzymes like lactate dehydrogenase, damage DNA, and ultimately lead to cell death [55]. More recently, Al-Shemy et al. [19] demonstrated that carboxylated cellulose nanocrystals–silver nano-biohybrids (CCN–Ag) exhibited strong antibacterial effects against various strains of *Listeria monocytogenes*. These biohybrids produced inhibition zones ranging from 16 to 19 mm, and concentrations between 0.25 and 1 µg/mL were sufficient to fully suppress bacterial growth.

Our results also showed that CS@AgP bio-nanocomposite demonstrated significant antifungal activity against *Candida albicans*, with inhibition zones increasing from 20 mm to 22 mm as the concentration rose from 6.25 to 25 mg/mL. This dose-dependent trend suggests enhanced disruption of fungal cell integrity at higher nanoparticle levels. Chitosan's antifungal mechanism is primarily attributed to its polycationic nature, which allows it to bind to negatively charged fungal cell membranes, increasing permeability and causing leakage of intracellular components [56]. Additionally, Ag_3PO_4 contributes silver ions and reactive oxygen species (ROS), which interfere with fungal respiration and DNA replication, amplifying the antifungal effect [57].

The observed synergy between chitosan and silver phosphate aligns with previous reports on chitosan-metal nanocomposites, which have shown broad-spectrum antimicrobial properties and potential for biomedical applications [58].

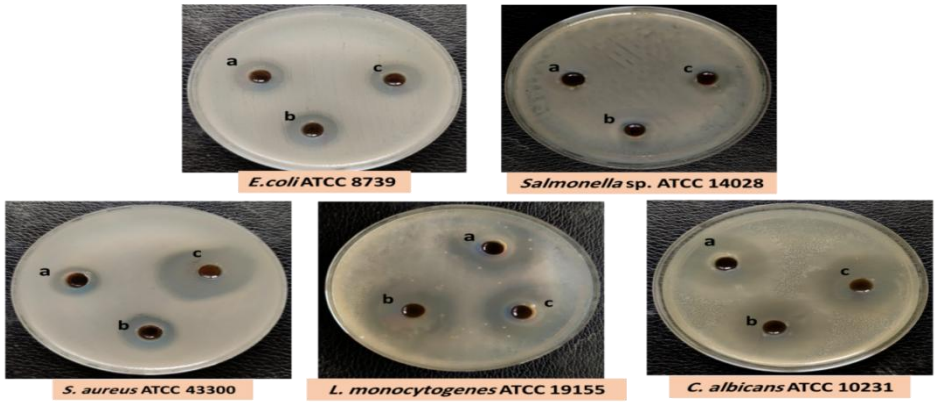

Figure 6. Antimicrobial activities of three concentrations (a) 6.25, (b) 12.5, and (c) 25 mg/ml CS@AgP against several pathogenic microorganisms.

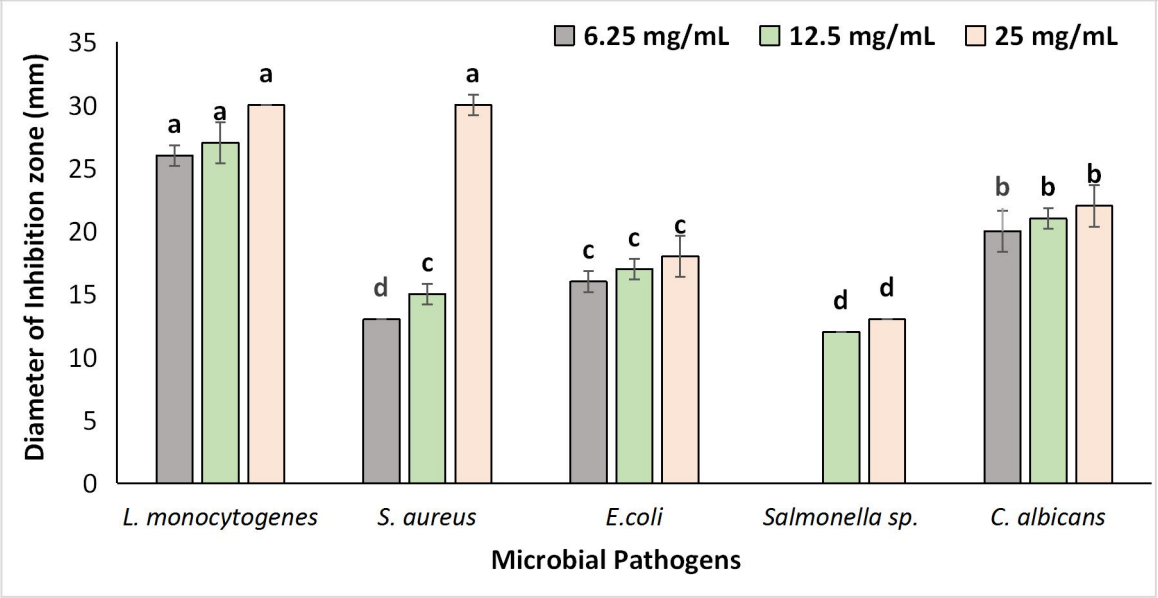

Figure 7. Inhibition zone diameter of a) 6.25, b) 12.5, c) 25 mg/mL CS@AgP bio-nanocomposite against several pathogenic microorganisms. [a,b] values in the above column with the same letter do not differ significantly according to Duncan's test at the 5% level. Bar indicated to ± standard deviation.

3. Experimental

3.1. Materials

Puparia of the black soldier fly (*Hermetia illucens*) were harvested from a local farm, washed thoroughly with distilled water to remove ash and surface contaminants, and dried overnight at 50°C. The dried puparia were then milled to ~10 mm particles using a mechanical grinder. Figure 8 presents a schematic of the Black Soldier Fly (*Hermetia illucens*) life cycle: egg (≈4 d), larva (≈14 d), pupa (puparium encasement ≈7–14 d), and adult (≈5–8 d), alongside the subsequent puparia pre-processing workflow. Analytical-grade sodium hydroxide (NaOH) and hydrochloric acid (HCl) were purchased from Abco-Chem and used as received, while anhydrous sodium tripolyphosphate (TPP) was obtained from Alpha Chemika.

3.1.1. Extraction of Chitosan

The chitosan extraction protocol, adapted from Dutta *et al.*, [27] proceeded as follows: *Hermetia illucens* puparia powder was demineralized in 1 M HCl for 24 h, washed to a neutral pH, and oven-dried. The dried material was then deproteinized in 1 M NaOH for 24 h and decolorized with $KMnO_4$ and oxalic acid to isolate pure chitin. Finally, the chitin was deacetylated under reflux in 50 % NaOH; this deacetylation step was repeated to maximize conversion to chitosan.

3.1.2. Preparation of CSNPs and CS@AgP Bio-Nanocomposite

Chitosan nanoparticles (**CSNPs**) were prepared by ionotropic gelation. In brief, 0.5 g of chitosan was dissolved in 100 mL of 1 % (v/v) acetic acid under stirring and the pH was adjusted to 4.6–4.8 with 1 N NaOH. CSNPs formed spontaneously when 3 mL of this chitosan solution was added dropwise into 1 mL of 0.25 % (w/v) TPP at room temperature (chitosan:TPP = 3:1 by mass). The resulting 200 mL suspension (0.3 % w/v) was sonicated for 5 min to ensure homogeneity. Neat CSNPs were isolated by centrifugation at 9 000 × g for 20 min, washed to a neutral pH and lyophilized [28].

For *in-situ* silver loading, 45 mL of 0.01 N $AgNO_3$ was added dropwise to the sonicated CSNP suspension at 50 °C under continuous stirring; the reaction was held for 2 h. The CS@AgP bio-nanocomposite was recovered by centrifugation at 10 000 × g for 15 min, rinsed with deionized water to remove residual reagents, and lyophilized.

3.2. Characterizations

Diffuse reflectance spectra (190–2500 nm) of CSNPs and CS@AgP bio-nanocomposite were recorded using a Jasco V-570 diffuse reflectance spectrophotometer (DRS mode). FT-IR spectra were acquired using a JASCO FT-IR 6100 (400–4000 cm^{-1} range, 4 cm^{-1} resolution, 64 scans). XRD patterns of the as-prepared materials were collected on a Malvern Panalytical Empyrean diffractometer (Cu Kα radiation, 2θ = 5–80°). Sample morphology and elemental composition were examined by FE-SEM (Quanta FEG-250, 20 kV) coupled with energy-dispersive X-ray spectroscopy (EDX).

3.3. Antimicrobial test

The antimicrobial activity of CS@AgP bio-nanocomposite at three concentrations, (a) 6.25, (b) 12.5, and (c) 25 mg/mL, was evaluated against Gram-positive bacteria (*Listeria monocytogenes* ATCC 7646, *Staphylococcus aureus* ATCC 6538), Gram-negative bacteria (*Escherichia coli* ATCC 25922, *Salmonella* sp. ATCC 14028), and unicellular fungi (*Candida albicans* ATCC 10231) using the agar diffusion method, following the procedure [29,30]. The bacteria were grown in a nutrient-liquid medium on a shaker bed at 200 rpm for 24 h at 37°C. The bacteria (1.5×10^8 CFU) were swabbed on Mueller-Hinton agar

plates; subsequently, 200 µL of the tested samples was deposited in wells (diameter of 7 mm) cut into agar plates. Then, agar plates were incubated at 37°C for 24 h. All the conducted studies were carried out in triplicate for all tested strains, where the inhibition zones surrounding the discs were quantified in millimeters.

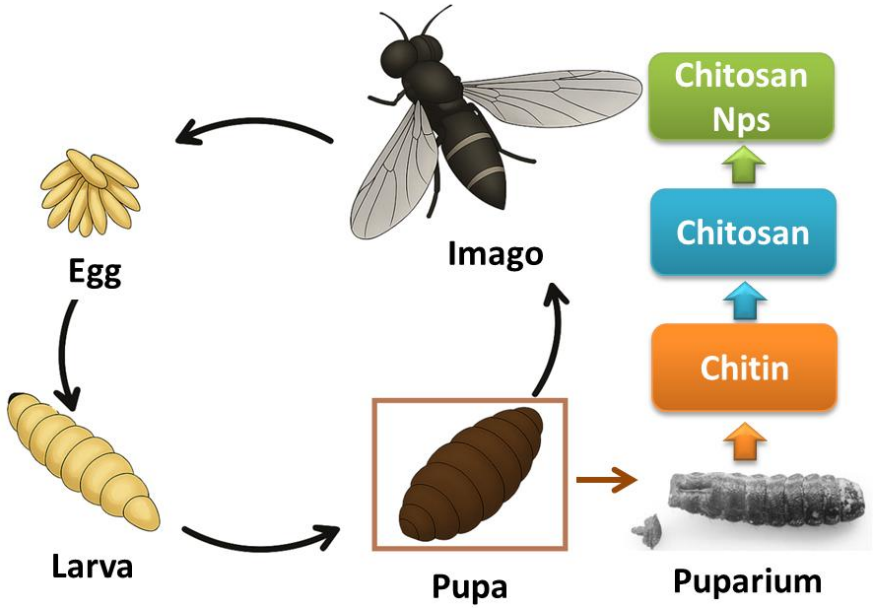

Figure 8. Schematic of the black soldier fly (*Hermetia illucens*) main life cycle and bioconversion of pupal chitin into chitosan nanoparticles.

3.4. Statistical analysis

Data were statistically determined using the IBM® SPSS® Statistics software version 21 on the premise of Duncan's multiple range test at the 5% level. All analyses were performed in triplicate.

4. Conclusions

The present study demonstrated a green, one-pot, tripolyphosphate-driven synthesis of Ag3PO4-decorated chitosan nanoparticles using black soldier fly puparia as a sustainable chitosan source. FTIR and XRD confirmed high-degree deacetylation of chitosan and in situ formation of crystalline Ag3PO4, while UV–Vis DRS/Tauc-plot analysis revealed a marked band-gap narrowing to 1.46 eV. EDX mapping further verified the chitosan matrix (C, N, O signatures), TPP crosslinking (P signature), and high-mass loading of silver, predominantly as phosphate domains, underscoring the robust coordination and hydrogen-bonding networks that stabilize the composite.

The resulting hierarchical CS@AgP architecture, with nanoscale Ag3PO4 domains uniformly embedded within an amorphous chitosan scaffold, enhances visible-light absorption, promotes efficient charge separation, and sustains Ag^+ release. These features translate to broad-spectrum, dose-dependent antimicrobial efficacy against Gram-positive, Gram-negative, and fungal pathogens, with inhibition zones up to 30 mm at 25 mg/mL. This dual-functional bio-nanocomposite holds promise for antimicrobial coatings and visible-light photocatalysis. Future studies will address cytotoxicity, photocatalytic pollutant degradation, and scale-up strategies to facilitate real-world applications.

5. Conflicts of interest

There are no conflicts to declare.

6. Formatting of funding sources

This work was financially supported by the National Research Centre, Egypt (Grant ID: 13010304).

7. Acknowledgments

The authors gratefully acknowledge the Faculty of Science, Benha University, for providing the necessary research facilities.

8. References and Bibliography

[1] Abdelhaq FEZM, Hasanin MS, Abdel-Monem MO, Abd El-Razek NM, Dacrory S, Dawwam GE. Highly Compatible Nanocomposite-Based Bacterial Cellulose Doped With Dopamine and Titanium Dioxide Nanoparticles: Study the Effect of Mode of Addition, Characterization, Antibacterial, and Wound Healing Efficiencies. Biopolymers 2025;116:e70025.

[2] Khasro A, Monem OA. Antibacterial Activity of Honey Bee Extract against Antibiotic Resistant Bacteria Isolated from Human Infections. Benha J Appl Sci 2022;7:125–32.

[3] Hahn T, Tafi E, Paul A, Salvia R, Falabella P, Zibek S. Current state of chitin purification and chitosan production from insects. J Chem Technol Biotechnol 2020;95:2775–95.
[4] Sheppard DC, Tomberlin JK, Joyce JA, Kiser BC, Sumner SM. Rearing methods for the black soldier fly (Diptera: Stratiomyidae). J Med Entomol 2002;39:695–8.
[5] Eggink KM, Dalsgaard J. Chitin contents in different black soldier fly (Hermetia illucens) life stages. J Insects as Food Feed 2023;9:855–64.
[6] Saravanan D, Gomathi T, Sudha PN. Comparative study of thermal stability using natural polymer blend by cross linking. Arch Appl Sci Res 2011;3:342–50.
[7] Guinesi LS, Cavalheiro ÉTG. The use of DSC curves to determine the acetylation degree of chitin/chitosan samples. Thermochim Acta 2006;444:128–33.
[8] Nasirov F, Abbasov V, Suleymanova E, Aslanbeyli A, Ahmedova S. Chitin and chitosan-biopolymer materials of the 21st century. Process Petrochemistry Oil Refin 2023;24: 778–824.
[9] Dash M, Chiellini F, Ottenbrite RM, Chiellini E. Chitosan—A versatile semi-synthetic polymer in biomedical applications. Prog Polym Sci 2011;36:981–1014.
[10] E Dawwam G, Mohamed F, El-Shall F, EL Awady M, Yassin M. A prospective chitosan produced from a biological source: Extraction, Characterization, and Assessment of biological performance. J Basic Environ Sci 2025;12:133–51.
[11] Anitha A, Chennazhi KP, Nair S V, Jayakumar R. 5-flourouracil loaded N, O-carboxymethyl chitosan nanoparticles as an anticancer nanomedicine for breast cancer. J Biomed Nanotechnol 2012;8:29–42.
[12] Majedi FS, Hasani-Sadrabadi MM, VanDersarl JJ, Mokarram N, Hojjati-Emami S, Dashtimoghadam E, Bonakdar S, Shokrgozar MA, Bertsch A, Renaud P. On-chip fabrication of paclitaxel-loaded chitosan nanoparticles for cancer therapeutics. Adv Funct Mater 2014;24:432–41.
[13] Wang B, Chen K, Jiang S, Reincke F, Tong W, Wang D, Gao C. Chitosan-mediated synthesis of gold nanoparticles on patterned poly (dimethylsiloxane) surfaces. Biomacromolecules 2006;7:1203–9.
[14] Fathy MM, M Omer A, Yaseen R, Abdel Salam SS, Dawwam GE. Myco-synthesis of silver and ZnO nanomaterials using endophytic fungi isolated from different locations in Egypt for sustainable development. J Basic Environ Sci 2024;11:745–54.
[15] Abd El-Gawad WM, Zaher KSA, Nawwar GAM. Exploring the utilities of rice straw black liquor (part XI): Enhancing the UV resistance, color, antimicrobial, and mechanical characteristics of epoxy coatings using lignin-based hybrid nano-pigments. Prog Org Coatings 2024;197:108866.
[16] Nawwar GAM, El-Ebiary NMA. Exploring the Utilities of Rice Straw Black Liquor:(Part X) Antioxidant/Antimicrobial New Sizing Additive for Brown Recycled Papers Properties Improvement. Afinidad J Chem Eng Theor Appl Chem 2025;82:377–84.
[17] Adel AM, Al-Shemy MT, Diab MA, El-Sakhawy M, Toro RG, Cerri L, Caschera D. Immobilization of TiO2NP@ oxidized cellulose nanocrystals for paper-based active packaging materials. Int J Biol Macromol 2023;231:123270.
[18] El-Sayed NS, Hashem AH, Kamel S. Preparation and characterization of Gum Arabic Schiff's bases based on 9-aminoacridine with in vitro evaluation of their antimicrobial and antitumor potentiality. Carbohydr Polym 2022;277:118823.
[19] Al-Shemy MT, El-Demerdash AS, Marzec A, Dawwam GE. Biocontrol of virulent Listeria monocytogenes using green carboxylated cellulose nanocrystals–silver nano-biohybrids. Int J Biol Macromol 2025;290:139012.
[20] Al-Shemy M, El-Shafie A, Alaneny A, Adel abeer. Facile In-Situ Synthesis of Nanocrystalline Celluloses-Silver Bio-nanocomposite for Chitosan Based Active Packaging. Egypt J Chem 2023; 66:335–52.
[21] Toro RG, Adel AM, de Caro T, Federici F, Cerri L, Bolli E, Mezzi A, Barbalinardo M, Gentili D, Cavallini M, Al-Shemy MT, Montanari R, Caschera D. Evaluation of Long–Lasting Antibacterial Properties and Cytotoxic Behavior of Functionalized Silver-Nanocellulose Composite. Materials (Basel) 2021;14:4198.
[22] Al-Shemy MT, Gamoń F, Al-Sayed A, Hellal MS, Ziembińska-Buczyńska A, Hassan GK. Silver nanoparticles incorporated with superior silica nanoparticles-based rice straw to maximize biogas production from anaerobic digestion of landfill leachate. J Environ Manage 2024;365:121715.
[23] Panáček A, Kolář M, Večeřová R, Prucek R, Soukupová J, Kryštof V, Hamal P, Zbořil R, Kvítek L. Antifungal activity of silver nanoparticles against Candida spp. Biomaterials 2009;30:6333–40.
[24] Nadworny PL, Wang J, Tredget EE, Burrell RE. Anti-inflammatory activity of nanocrystalline silver in a porcine contact dermatitis model. Nanomedicine Nanotechnology, Biol Med 2008;4:241–51.
[25] Rogers J V, Parkinson C V, Choi YW, Speshock JL, Hussain SM. A preliminary assessment of silver nanoparticle inhibition of monkeypox virus plaque formation. Nanoscale Res Lett 2008;3:129.
[26] Gurunathan S, Kalishwaralal K, Vaidyanathan R, Venkataraman D, Pandian SRK, Muniyandi J, Hariharan N, Eom SH. Biosynthesis, purification and characterization of silver nanoparticles using Escherichia coli. Colloids Surfaces B Biointerfaces 2009;74:328–35.
[27] Dutta PK, Dutta J, Tripathi VS. Chitin and chitosan: Chemistry, properties and applications. J Sci Ind Res 2004;63:20–31.
[28] Debnath S, Suresh Kumar R, Niranjan Babu M. Ionotropic gelation - A novel method to prepare chitosan nanoparticles. Res J Pharm Technol 2011;4:492–5.
[29] Dawwam GE, Al-Shemy MT, El-Demerdash AS. Green synthesis of cellulose nanocrystal/ZnO bio-nanocomposites exerting antibacterial activity and downregulating virulence toxigenic genes of food-poisoning bacteria. Sci Rep 2022;12:16848.
[30] El-Sayed NS, Dawwam GE, Helmy NM, Hesemann P, Kamel S. Encapsulation of ZnO-NPs, tannic acid, and β-carotene into cellulose coated polydopamine bionanoplatform: Fabrication, characterization, antimicrobial, and in vitro wound healing evaluation. Int J Biol Macromol 2025:145928.

[31] Soetemans L, Uyttebroek M, Bastiaens L. Characteristics of chitin extracted from black soldier fly in different life stages. Int J Biol Macromol 2020;165:3206–14.
[32] Tan YN, Chin YL, Chen WN. Comparison of Sustainable Lipid and Protein Removal Methods for the Isolation of Insect Chitin from Black Soldier Fly Exoskeleton. ACS Food Sci Technol 2021;1:698–706.
[33] Mirwandhono E, Yunilas, Ginting N, Siregar GAW, Nasution MIA, Wahyuni S, Siswanto. Isolation and characterization of chitosan from black soldier fly exuviae. IOP Conf Ser Earth Environ Sci 2024;1362:0–5.
[34] Abdelmoniem SA, Faheim AA, Al-Shemy MT, Abd El-Wahab ZH. Synthesis and characterization of cellulose microcrystals–chromium oxide nanocomposites: Enhancing surface, thermal, and optical properties. Egypt J Chem 2025; 68: 749-65.
[35] Hassan MA, Al-Shemy MT, Kamal KH, Strachota B, Strachota A, Pavlova E, Konefał M, Kamel S. Hydrogel-activated hydrochar synergy for efficient wastewater purification: tackling Imidacloprid pesticides and crystal Violet dye. Appl Water Sci 2025;15:197.
[36] Marangon A, Paul G, Zaghi R, Marchese L, Gatti G. Chitin Extracted from Black Soldier Fly Larvae at Different Growth Stages. Polymers 2024; 16:2861.
[37] Dassanayake RS, Acharya S, Abidi N. Biopolymer-Based Materials from Polysaccharides: Properties, Processing, Characterization and Sorption Applications. Adv. Sorption Process Appl., IntechOpen; 2019.
[38] Mahmoud DS, Zaher KSA, El-Sabbagh SH, Yossef AM, Nawwar GAM. Using of aluminum (lignin/silica/fatty acids) hybrid filler in the fabrication of natural rubber conductive elastomers. Sci Rep 2025;15:25363.
[39] Putri SE, Ahmad A, Raya I, Tjahjanto RT, Irfandi R. Synthesis and antibacterial activity of chitosan nanoparticles from black tiger shrimp shells (Penaeus monodon). Egypt J Chem 2023;66:129–39.
[40] Xiong S, Liu M, Yan J, Zhao Z, Wang H, Yin X, Wang L, Chen S. Immobilization of Ag3PO4 nanoparticles on chitosan fiber for photocatalytic degradation of methyl orange. Cellulose 2018;25:5007–15.
[41] Alhokbany NS, Mousa R, Naushad M, Alshehri SM, Ahamad T. Fabrication of Z-scheme photocatalysts g-C3N4/Ag3PO4/chitosan for the photocatalytic degradation of ciprofloxacin. Int J Biol Macromol 2020;164:3864–72.
[42] El-Sayed NS, Tolba E, Salama A. Valorization of Sugarcane Bagasse into Cellulose Nanofiber Containing Phosphate Groups: A New Scaffold for in Vitro Calcium Phosphate Mineralization. Chem Africa 2025:1–11.
[43] Liang Q, Ma W, Shi Y, Li Z, Yang X. Hierarchical Ag 3PO 4 porous microcubes with enhanced photocatalytic properties synthesized with the assistance of trisodium citrate. CrystEngComm 2012;14:2966–73.
[44] Sulaeman U, Permadi RD, Ningsih DR, Diastuti H, Riapanitra A, Yin S. The surface modification of Ag3PO4 using anionic platinum complexes for enhanced visible-light photocatalytic activity. Mater Lett 2020;259:126848.
[45] Adel AM, El-Shall FN, Diab MA, Al-Shemy MT. Biogenic silver-doped mesoporous silica nanoparticles for multifunctional eco-designed textile printing. Biomass Convers Biorefinery 2024; 14:27905–23.
[46] El-Sayed NS, Moussa MA, Kamel S, Turky G. Development of electrical conducting nanocomposite based on carboxymethyl cellulose hydrogel/silver nanoparticles@polypyrrole. Synth Met 2019;250:104–14.
[47] Ashraf MA, Li C, Zhang D, Zhao L, Fakhri A. Fabrication of silver phosphate-ilmenite nanocomposites supported on glycol chitosan for visible light-driven degradation, and antimicrobial activities. Int J Biol Macromol 2021;169:436–42.
[48] Lu Y, Zhu S, Huang E, He Y, Ruan J, Liu G, Yan H. Pressure-driven band gap engineering in ion-conducting semiconductor silver orthophosphate. J Mater Chem A 2019;7:4451–8.
[49] Thamilarasan V, Sethuraman V, Gopinath K, Balalakshmi C, Govindarajan M, Mothana RA, Siddiqui NA, Khaled JM, Benelli G. Single Step Fabrication of Chitosan Nanocrystals Using Penaeus semisulcatus: Potential as New Insecticides, Antimicrobials and Plant Growth Promoters. J Clust Sci 2018;29:375–84. https://doi.org/10.1007/s10876-018-1342-1.
[50] Canbolat F, Acar İ, Tezel RN. Development of chitosan nanoparticle loaded with Tricholoma fracticum extract and evaluation of in vitro antioxidant activity. Int J Food Sci Technol 2024:7971–86.
[51] Klein J, Kampermann L, Mockenhaupt B, Behrens M, Strunk J, Bacher G. Limitations of the Tauc Plot Method. Adv Funct Mater 2023;33:1–19.
[52] Yi Z, Ye J, Kikugawa N, Kako T, Ouyang S, Stuart-Williams H, Yang H, Cao J, Luo W, Li Z, Liu Y, Withers RL. An orthophosphate semiconductor with photooxidation properties under visible-light irradiation. Nat Mater 2010;9:559–64.
[53] Tsai G-J, Su W-H. Antibacterial activity of shrimp chitosan against Escherichia coli. J Food Prot 1999;62:239–43.
[54] Raafat D, Von Bargen K, Haas A, Sahl H-G. Insights into the mode of action of chitosan as an antibacterial compound. Appl Environ Microbiol 2008;74:3764–73.
[55] Pellieux C, Dewilde A, Pierlot C, Aubry J-M. Bactericidal and virucidal activities of singlet oxygen generated by thermolysis of naphthalene endoperoxides. Methods Enzymol., vol. 319, Elsevier; 2000, p. 197–207.
[56] Goy RC, Britto D de, Assis OBG. A review of the antimicrobial activity of chitosan. Polímeros 2009;19:241–7.
[57] Marambio-Jones C, Hoek EM V. A review of the antibacterial effects of silver nanomaterials and potential implications for human health and the environment. J Nanoparticle Res 2010;12:1531–51.
[58] Ahmed S, Ali A, Sheikh J. A review on chitosan centred scaffolds and their applications in tissue engineering. Int J Biol Macromol 2018;116:849–62.